# Structure and anisotropy of the Mexico subduction zone based on Rayleigh-wave analysis and implications for the geometry of the Trans-Mexican Volcanic Belt

I. Stubailo,[1] C. Beghein,[1] P. M. Davis,[1]

Corresponding author: I. Stubailo (stubailo@ess.ucla.edu)

[1]Department of Earth and Space Sciences,

University of California Los Angeles,CA

90095,USA.

**Abstract.** We develop a three-dimensional model of shear-wave velocity and anisotropy for the Mexico subduction zone using Rayleigh wave phase velocity dispersion measurements. This region is characterized by both steep and flat subduction and a volcanic arc that appears to be oblique to the trench. We give a new interpretation of the volcanic arc obliqueness and the location of the Tzitzio gap in volcanism based on the subduction morphology.

We employ the two-station method to measure Rayleigh phase velocity dispersion curves between periods of 16 s to 171 s. The results are then inverted to obtain azimuthally anisotropic phase velocity maps and to model 3-D variations in upper mantle velocity and anisotropy. Our maps reveal lateral variations in phase velocity at all periods, consistent with the presence of flat and steep subduction. We also find that the data are consistent with two layers of anisotropy beneath Mexico: a crustal layer, with the fast directions parallel to the North American absolute plate motion, and a deeper layer that includes the mantle lithosphere and the asthenosphere, with the fast direction interpreted in terms of toroidal mantle flow around the slab edges.

Our combined azimuthal anisotropy and velocity model enables us to analyze the transition from flat to steep subduction and to determine whether the transition involves a tear resulting in a gap between segments or is a continuous deformation caused by a lithospheric flexure. Our anisotropy results favor a tear, which is also consistent with the geometry of the volcanic belt.

## 1. Introduction

The evolution, origin, and structure of the Mexican subduction zone have been studied using a variety of techniques over the years (e.g., *Truchan et al.*, 1973; *Pardo and Suarez*, 1995; *Manea et al.*, 2005; *Kanjorski*, 2003). Global plate reconstruction indicates that the Farallon plate fragmented about 23 Ma ago, at which point two new plates were created: the Cocos plate to the North and the Nazca plate to the South (*Atwater and Stock*, 1998; *Mann et al.*, 2007; *Londsdale*, 1991). About 13 Ma later, the Rivera plate came into existence by separating from the Cocos plate.

Based on seismicity, focal mechanisms, and the slab geometry determined from the hypocenter locations of local events, the area under Mexico can be split into several sections (*Pardo and Suarez*, 1995): (1) the Jalisco section, where the Rivera plate subducts steeply at approximately 50°, (2) the Michoacan section, where the dip of the Cocos plate undergoes a transition from steep to almost parallel to the surface, (3) the Guerrero-Oaxaca section, where the slab is flat for about 250 km, and (4) the southern Oaxaca and Chiapas section, where the dip of the Cocos plate increases up to 30°. As a result of the complex subduction, the Trans-Mexican Volcanic Belt (TMVB), which consists of nearly 8000 volcanoes, is apparently oblique to the Trench instead of being parallel to it (Figure 1).

Detailed information on the slab depth under the transect from Acapulco to Tampico has been obtained from the teleseismic data collected during the Middle America Subduction Experiment (MASE) (*Perez-Campos et al.*, 2008; *Husker*, 2008; *Iglesias et al.*, 2010). The results based on receiver function analysis (*Perez-Campos et al.*, 2008) and body wave tomography (*Husker*, 2008; *Husker and Davis*, 2009) show an approximately 40 km thick, flat, shallow slab, that starts dipping 250 km inland from the trench at approximately a 74° angle, and that is truncated at 500 km depth. The flat subduction under the MASE array is consistent with the prior study by *Pardo and Suarez* (1995). A two-dimensional (2-D) slab image based on the S-wave velocity was also obtained by *Iglesias et al.* (2010) using regional earthquakes. The authors described a well-resolved low-velocity zone below the TMVB consistent with the presence of a mantle wedge. *Chen and Clayton* (2009) showed low attenuation associated with the subducting part of the slab (forearc) and high attenuation near the mantle wedge and beneath the TMVB. The authors interpeted the high-attenuation zone in the mantle wedge as related to relatively high temperature, fluids, and partial melts produced during the subduction process. The current 2-D view of the slab under the Central Mexico region (MASE line) based on those prior studies (*Kim et al.*, 2006; *Husker*, 2008) is shown in Figure 2.

In this study, we use data from networks with unprecedented dense coverage to develop a 3-D model of S-wave velocity and azimuthal anisotropy of the Mexican subduction zone. The azimuthal anisotropy is the dependence of local seismic propagation characteristics on the azimuth of propagation. The 3-D nature of our results allows for better understanding of the interaction between the subducting slab, the mantle lithosphere, and the asthenosphere.

Seismic anisotropy is important to study since it can provide insights into the deformation history of the region. It may arise from the lattice preferred orientation (LPO) of intrinsically anisotropic crystals or from the shape preferred orientation of isotropic materials with contrasting elastic properties (*Karato*, 1998). Anisotropy in the crust may be caused by mineral fabrics, preferentially oriented fluid-filled cracks, and the presence of faults (*Crampin et al.*, 1984). In the upper mantle, it is often attributed to the LPO of olivine over large scales, and therefore can give information on the past and current deformation processes in the lithosphere and asthenosphere, respectively (*Karato*, 1998; *Silver*, 1996).

To obtain a 3-D model of the Mexican subduction zone, we perform dispersion measurements of Rayleigh waves for periods of 16-171 s and show that Rayleigh phase velocities depend on the azimuth of propagation. The dense network of seismic stations used here and the analysis based on surface waves, which inherently have better depth sensitivity to structure than body waves, allow us to obtain a higher-resolution velocity and anisotropy model than in previous studies. The combined 3-D models of S-wave velocities and anisotropy enable us to infer information about the dynamics of the subduction process in the region.

## 2. Data

We use data collected by several networks on a total of 181 stations (Figure 3): the Mesoamerican Seismic Experiment (MASE, 100 stations), the Network of Autonomously Recording Seismographs (NARS, 15 stations), USArray (24 stations), Mapping the Rivera Subduction Zone (MARS, 9 stations), and the Mexican Servicio Sismologico Nacional (SSN, 33 stations). All the Z-component waveforms used are down-sampled to 1 sample per second and corrected for the instrument response to eliminate phase distortion at higher frequencies.

Our data selection is tailored to the two-station method (*Sato*, 1955; *Brune and Dorman*, 1963; *Knopoff et al.*, 1967; *Herrmann*, 1987), which allows us to measure phase velocities between two stations that share a common great-circle path with an event. This method has the advantage over single-station phase velocity measuring techniques of removing uncertainties related to the source and to the path between the source and its near station. The codes employed here are based on the method developed by *Herrmann* (1987) as implemented by J. A. Snoke (*Warren et al.*, 2008). We identify combinations of station pairs and events for which the angles between the great circles are no larger than 3° (Figure 4). To have suitable signal-to-noise ratio (SNR), we further restrict ourselves to events with moment magnitude 6.0 and larger in the USGS catalog and depths shallower than 250 km.

We perform a frequency-time analysis (FTAN) (*Landisman et al.*, 1969; *Dziewonski et al.*, 1969) for each earthquake and station. We use the FTAN plots to narrow down both a range of group velocities and periods suitable for further processing in order to isolate the fundamental mode surface waves. A time window was then determined for each period range based on the group velocity range and epicentral distance.

Events and stations with low signal-to-noise ratio or irregular FTAN plots (Figure 5) are rejected. We also reject pairs of stations for which the phase velocities differ for earthquakes arriving from opposite sides. For instance, if the phase velocity determined for station pair STA1-STA2 does not fall within the uncertainties estimated for the phase velocity of station pair STA2-STA1, the measurements for that station pair are rejected. Such phase velocity discrepancies can be caused by paths that cross tectonic boundaries at sharp angles leading to refraction, multipathing, and scattering. Of all the station pairs that were associated with events coming from opposite directions, only a small number (20 %) were rejected and the majority of these rejected pairs were originated from Peru, Chile, and Western Canada, i.e., from GCPs parallel to the coastline. *Tanimoto and Prindle* (2007) showed that for waves propagating along such paths, off-great-circle path propagation can affect estimates of azimuthal anisotropy from Rayleigh waves by up to 30°. However, for paths that are roughly perpendicular to the coastline, they showed that off-great-circle path effects were negligible. Because of this, and since most of our events have GCPs perpendicular to the coastline (see Figure 4), we do not think the inversion results would be affected significantly.

## 3. Interstation phase velocity measurements

Based on the criteria described in Section 2, we are able to identify 7602 station pairs corresponding to 116 teleseismic events recorded between 2005 and 2009. If a pair of stations is linked to multiple events, we average the dispersion curve measurements. After averaging the dispersion curves, we are left with 5050 interstation phase velocity curves (with up to 12 events per path) for the periods of 16, 18, 20, 22, 25, 28, 33, 38, 44, 54, 68, 85, 102, 128, and 171 seconds. The path density for the selected events is higher to the west of the study area (Figure 3), but overall the selected paths result in excellent coverage as shown by the resolution tests described in Section 4.

The interstation method employed uses a reference phase velocity spectrum calculated for a local reference Earth model to remove the need for phase unwrapping. Our local reference Earth model (hereafter referred to as mTNA) is a composite model, modified from the upper mantle shear-wave velocity Tectonic North America (TNA) model (*Grand and Helmberger*, 1984) by adding the P-wave velocities and densities from model AK135 (*Kennett et al.*, 1995), and the Crust 2.0 crustal model (*Bassin et al.*, 2000). This reference model is shown in Figure 6 and described in Table 1. Phase velocity uncertainties are determined based on the coherence of the two waveforms after the near-station waveform has been time-shifted to the far-station epicentral distance using the calculated phase velocities (see details in *Warren et al.*, 2008).

Examples of interstation measurements made along the MASE array at three different locations with respect to the slab are shown in Figure 7. The interstation phase velocity measurements vary systematically along the MASE array, with a decrease in phase velocity from southwest to northeast, away from the subducting slab. The higher phase velocities are thus located above the region of flat slab subduction, consistent with the tomographic body-wave inversion of *Husker and Davis* (2009).

## 4. Azimuthally anisotropic phase velocity maps

### 4.1. Method

The two-station technique employed here enables us to measure path-averaged phase velocities $\bar{c}$ between two stations:

$$\bar{c}(T) = \frac{1}{d_2 - d_1} \int_{d_1}^{d_2} c(T, l) dl \quad (1)$$

where $T$ indicates the period considered, and stations 1 and 2 are located along the great-circle path $l$ at epicentral distances $d_1$ and $d_2$, respectively. We invert our path-averaged phase velocity measurements using the least-squares (LSQR) method developed by Lebedev (*Darbyshire and Lebedev* (2009)) and previously employed by *Beghein et al.* (2010). With this method, the study area is parameterized by a 2-D triangular grid. The choice of the grid spacing is subjective, but the spacing should remain smaller than the features we are trying to resolve, which themselves depend on the station spacing and the azimuthal coverage achieved. Cells that are too large would smooth the data unnecessarily and potentially hide interesting model features, while cells that are too small could display variations that are not resolvable with our data. After testing parameterization with 45, 60, and 100 km spacing, we select the grid spacing of 60 km (for the total of 898 grid cells).

This method not only enables us to obtain isotropic phase velocity maps at different periods, but also allows us to model the azimuthal dependence of the phase velocity. In a slightly anisotropic medium, phase velocities can be expressed as (*Smith and Dahlen*, 1973):

$$c(T,\Psi) = c_0(T) + c_1(T)cos(2\Psi) + c_2(T)sin(2\Psi) + c_3(T)cos(4\Psi) + c_4(T)sin(4\Psi) \quad (2)$$

where $c$ is the phase velocity, $T$ is the period, $\Psi$ is the azimuth, $c_0(T)$ is the isotropic term, and $c_{1-4}$ are the azimuthal coefficients (*Backus*, 1970). The directions $\Theta$ of fast propagation for Rayleigh waves and the amplitude $A$ of the anisotropy can be obtained using :

$$\Theta_{2\Psi} = 1/2 \arctan(c_2/c_1), \quad (3)$$

$$\Theta_{4\Psi} = 1/4 \arctan(c_4/c_3), \quad (4)$$

$$A_{2\Psi} = \sqrt{(c_1^2 + c_2^2)}, \quad (5)$$

$$A_{4\Psi} = \sqrt{(c_3^2 + c_4^2)}. \quad (6)$$

Like most geophysical inverse problems, the inversion of Eq. 1 is non-unique, which means that a subjective regularization must be imposed. The anisotropic and isotropic terms are smoothed independently, and each period is treated separately from the others. We use the trade-off curves (or L-curves) to choose a damping value for each period (Figure 8). The preferred damping is chosen near the corner of the L-curve. After a damping value is chosen for the isotropic term, we proceed with varying the damping for the anisotropic terms (first the $2\Psi$ terms, then the $4\Psi$ terms, independently). Even though dispersion curves are obtained for periods between 16 s and 171 s, our ray coverage is not sufficient to reasonably resolve phase velocity anomalies at periods greater than 100 s (a large damping is needed and no significant variation in phase velocity is found). We thus focus the rest of the manuscript on the results obtained at periods between 16 s and 100 s.

To evaluate the significance of the reduction in misfit $\chi^2$ when adding anisotropy, we perform standard F-tests (*Bevington and Robinson*, 1992) following the method described by *Trampert and Woodhouse* (2003): we vary the damping and compute the $\chi^2$ misfit and the trace of the resolution matrix $\mathbf{R}$ for the isotropic model, for the $0\Psi+2\Psi$ model, and for the model that includes all anisotropic terms ($0\Psi$, $2\Psi$, and $4\Psi$).

The resolution matrix $\mathbf{R}$, which is not readily calculated by the LSQR method, is determined for various damping values following *Trampert and Woodhouse* (2003). Each column $j$ of the matrix $\mathbf{G}$ that describes the physical relation between the data and the model parameters is inverted:

$$R_j = \mathbf{L}G_j \tag{7}$$

where $R_j$ is column $j$ of matrix $\mathbf{R}$, $\mathbf{L}$ is the LSQR operator, and $G_j$ is column $j$ of matrix $\mathbf{G}$. In our case, $\mathbf{R}$ is a 4490x4490 matrix, with 898 rows and columns for the isotropic part, 1796 rows and columns containing $2\Psi$ sin and cos components, and 1796 rows and columns with $4\Psi$ sin and cos components (see Eq. 2). Figure 9 displays $\chi^2$ as a function of the trace of $\mathbf{R}$ for the isotropic and anisotropic inversions for the period of 28 s. This Figure, combined with the F-tests, shows that the $2\Psi$ terms are needed to explain the data, but the $4\Psi$ terms do not improve the data fit significantly. We obtain similar outcomes for the other periods. Hence, in the following, we discuss only the isotropic ($0\Psi$) and $2\Psi$ terms.

To evaluate the quality of our data coverage, we conduct isotropic and anisotropic resolution tests for all periods. Figures 10 and 11 show three representative tests at a period of 44 s : (1) a test of the isotropic inversion with a checkerboard input (Figure 10), (2) a test of the anisotropic inversion with a purely isotropic input (Figure 11, A and B), and (3) a test of the anisotropic inversion where the input has variations in both isotropic velocity and anisotropy (Figure 11, C and D). In the anisotropic tests, the isotropic inputs are chosen to coincide with our preferred phase velocity model at the period considered. Figures 10 and 11 demonstrate that the input isotropic and anisotropic models are well recovered in the middle of the study area, close to the MASE array, marked by the green line on the figures, with some discrepancies and smearing north of 21° latitude and east of 96° longitude (shaded area in the figures). We find that an anisotropic inversion of an isotropic input model (Figure 11A and B) yields an output model with virtually no anisotropy (less than 0.5%) everywhere in the study area. Because the resolution of our models is better in the center of our study area, where the number of stations, and therefore the number of crossing paths, is higher, we will concentrate the discussion of the results on that part of the region.

Trade-offs between isotropic and anisotropic terms in the inversion of Eq. 1 can affect the results. The synthetic tests shown in Fig. 11A and B demonstrate that our inversion scheme can detect the absence of anisotropy, and therefore that there is little trade-off between the isotropic and anisotropic terms. Another way to analyze these trade-offs is by computing the resolution matrix **R** from Eq. 7, which we do using the damping values chosen for our preffered anisotropic model (Figure 12). Each line of **R** corresponds to a model parameter, and the matrix is divided into nine sub-matrices $c_i c_j$ $(i, j = 0, 1, 2)$, where $c_0$ spans parameters that correspond to the $0\Psi$ term, and $c_1$ and $c_2$ span parameters that correspond to the two $2\Psi$ terms. The off-diagonal submatrices $c_i c_j$ $(i \neq j)$, represent trade-offs between the three terms, and the off-diagonal elements within the submatrices $c_i c_i$ indicate lateral trade-offs, i.e., trade-off within the same $c_i$ term but at different geographic locations. Figure 12 shows the existence of some lateral trade-offs, which result from imperfect ray coverage and lateral smoothing. It also demonstrates that trade-offs exist between the isotropic and anisotropic terms and between the two $2\Psi$ terms, but that they are relatively small. The synthetic tests performed in addition to the resolution matrix shown here give us confidence in the significance and resolution of the obtained anisotropy.

### 4.2. Results

The obtained phase velocity maps are shown in Figure 13 for periods of 18 s, 44 s, and 85 s. The results reveal lateral variations in isotropic phase velocities at all periods, consistent with the presence of a flat slab: phase velocities are generally larger than average in the forearc, and lower than average near the TMVB. At short periods (16 s-33 s), there are strong lateral variations in phase velocities and anisotropy. Considering the depth sensitivity of Rayleigh waves at these periods (see sensitivity kernels in Figure 14), these rather complex variations may reflect changes in the crustal and mantle lithospheric structure, and deformation history. At periods of 38 s and higher, the phase velocity anomalies and anisotropy are smoother. It is remarkable to note that the transition between the faster and slower than average phase velocities follows the isodepth lines of the local seismicity, both in the flat and steeper portions of the slab.

We also find an east-west variation in phase velocity anisotropy at all periods, and a change in the fast direction between the forearc and the backarc. Both findings are likely to be the signature of complex 3-D deformation at depth. Interestingly, at periods of 38 s and higher, the fast direction of propagation in the western part of our study region is perpendicular to the trench near the coast. In the southeast, the fast direction found above the slab is subparallel to the trench at most periods. In the backarc, azimuthal anisotropy is present at all periods up to 85 s, with the fast direction of propagation often at a steep angle to the strike of the arc. Considering that at periods larger than 33 s our data are mostly sensitive to structure below 50 km depth (Figure 14), and considering previous estimates of the slab geometry from body wave data (*Husker and Davis, 2009*), the orientation of the fast direction likely reflects lithospheric and/or asthenospheric deformation.

## 5. Three-dimensional models

### 5.1. Shear-wave velocity structure

Phase velocities provide only a depth-integrated image of the upper mantle. In order to obtain a 3-D model, we need to invert the phase velocity maps for shear wave velocity and anisotropy.

Perturbations in the isotropic part of the phase velocity $c_0$ correspond to the depth average of perturbations in shear-wave velocity ($\delta V_S$), P-wave velocity ($\delta V_P$), and density ($\delta\rho$) weighted by sensitivity kernels (Figure 14):

$$\delta c_0 = \int_0^a [K_{V_S}(r)\delta V_S(r) + K_{V_P}(r)\delta V_P(r) + K_\rho(r)\delta\rho(r)]dr \tag{8}$$

where $a$ represents the radius of the Earth, and $K_m(r)$ is the phase velocity sensitivity kernel or partial derivative with respect to model parameter $m$ (here $m$ stands for $V_S$, $V_P$, and $\rho$).

In this work, the isotropic part of the phase velocity maps is inverted for $V_S$ via a linearized least-squares inversion using code *surf96* (*Herrmann*, 1987; *Herrmann, Ammon*, 2002). We impose a depth parameterization in terms of three layers down to 200 km depth, with the top layer representing the crust and the other two layers being located in the mantle (Figure 15D). The middle layer spans depths going from the Moho, as constrained by receiver function analyses (see explanations below), to 100 km depth. We choose approximately 50-60 km as the average lithosphere thickness based on the subducting plate age (*Turcotte and Schubert*, 1982; *Husker and Davis*, 2009) since the slab is too young and hot to distinguish between the lithosphere and asthenosphere based on seismic methods (*Perez-Campos et al.*, 2008). Like most geophysical inverse problems, inversions of surface wave phase velocities to constrain $V_S$ are inherently non-unique. Part of the non-uniqueness arises from the existence of trade-offs between the Moho depth and velocity structure. Therefore, to reduce the number of models that can explain the data, and because receiver function analyses are better suited than surface waves to constrain crustal thickness, we impose a priori constraints on the Moho depth based on the work by *Kim and Clayton* (personal communication). Since the Moho depths are only determined where seismic stations are located, we interpolate the data where no receiver function information is available. The Moho depth is thus laterally variable and so is the thickness of the two top layers of the model. The initial values of density and $V_P$ for the inversion are assigned based on the reference model mTNA (Table 1); for each layer of our model (Figure 15D), we average the values from mTNA within the same depth range. During the inversion, the $V_P/V_S$ ratio is kept fixed.

Herrmann's method uses differential smoothing during the inversion, which means that it damps the differences between $V_S$ in adjacent layers. After investigating a range of values for the damping parameter, we choose to start with a damping of 10% of the maximum eigenvalue of the data kernel, decreasing it to 3% after five iterations in the total of 30 iterations. The selection of the damping values and number of iterations is based on the final solution stability and improvement in misfit.

The depth inversions are carried out at every grid cell that parametrizes the study area (Section 4), and the resulting shear-wave velocity profiles are combined to form a 3-D $V_S$ model of the region as displayed in Figure 15. Our model shows lateral variations in $V_S$ at all depths, with larger values in the south of the study region, most likely reflecting the presence of the slab, and slightly lower in the northern part of the region. We find lateral variations in $V_S$ of approximately 0.3 km/s in the mantle and crust. Note that, since our 3-D $V_S$ model results from the inversion of phase velocity maps that are themselves generated by inversion of dispersion measurements, our $V_S$ model amplitude is indirectly affected by the smoothing applied during the construction of the phase velocity maps. A lower damping of the shortest period dispersion data may have resulted in stronger phase velocity anomalies and stronger crustal $V_S$.

### 5.2. Azimuthal anisotropy

At a given period $T$, the phase velocity azimuthal anisotropy relates to azimuthal anisotropy at depth through equations similar to Eq. 8 :

$$c_1 = \int_0^a K_G G_c dr \tag{9}$$

$$c_2 = \int_0^a K_G G_s dr \tag{10}$$

where $c_1$ and $c_2$ are the $2\Psi$ anisotropic terms of Eq. 2, $G_c$ and $G_s$ are elastic parameters that describe the azimuthal anisotropy of vertically polarized shear-waves, and $K_G$ describes the sensitivity of Rayleigh waves to $G_c$ and $G_s$.

We invert Eqs. 9 and 10 for $G_c(r)$ and $G_s(r)$ using a singular value decomposition (SVD) method. We follow the procedure described by *Matsu'ura and Hirata* (1982) to determine how many eigenvalues to keep in the reconstruction of the model. The inversion is done over the same layers used for the inversion of the isotropic term. After obtaining a model for $G_s$ and for $G_c$, we calculate the amplitude $A$ of the anisotropy and the fast direction of propagation $\Theta$ for vertically polarized shear-waves at every grid cell and in every layer using :

$$A = \sqrt{(G_c^2 + G_s^2)} \tag{11}$$

$$\Theta = 1/2\,\arctan(G_s/G_c) \tag{12}$$

The results are displayed in Figure 15. In our interpretation, we concentrate on the patterns in the mantle lithosphere and asthenosphere (Figure 15B,C). Unlike most subduction zones that display anisotropy with the fast direction parallel to the trench (*Long and Silver*, 2008), our results show a more complex pattern of anisotropy, with the fast azimuth of propagation perpendicular to the trench northwest of MASE and almost parallel to the trench in the southeast (Figure 15B, C). There is a clear and sharp near-vertical transition between 45 and 200 km depth showing 0.5-2 % variations in anisotropy with higher amplitudes where the fast direction is parallel to the trench. In the crust (Figure 15A), we observe a complex anisotropy pattern. Overall, the crustal anisotropy does not coincide with that of either mantle lithosphere (Figure 15B) or asthenosphere (Figure 15C). This is not surprising, since anisotropy at different depth likely has different origins (Lin et al., 2010; Yang et al., 2011): the anisotropy in the crust correlates with geologic/tectonic features whereas the anisotropy in the upper mantle depends on temperature variations and mantle flow. A similar variation in anisotropic behavior with depth is also observed in the western United States (Lin et al., 2010; Yang et al., 2011).

Our anisotropy results combined with our S-wave velocity model enable us to obtain new insights into the Mexico subduction zone, as discussed in the next section.

## 6. Discussion

### 6.1. Evidence for tear in the slab along OFZ

Our results confirm the conclusions of prior studies (*Kanjorski*, 2003; *Pardo and Suarez*, 1995; *Blatter at al.*, 2007) that the angle of subduction varies substantially along the trench. There are several distinctive features observed with $V_S$ that vary gradually between layers in Figure 15D. The higher velocities of 4.4 km/s are seen in the middle layer (Figure 15B) in the subduction zone near the coast, extending inland beneath the southern part of the MASE array. We associate these higher velocities with the slab subduction, specifically with a shallow flat slab under the MASE and a steep slab to the west of it. This finding is consistent with the shallow slab location determined by *Pardo and Suarez* (1995), *Perez-Campos et al.* (2008), *Husker* (2008), and *Husker and Davis* (2009) based on seismicity patterns, receiver function tomography, and P-wave tomography, respectively. The slabs at the depths of up to 100 km appear to be almost disconnected.

Another striking feature is a low velocity zone in the northern part of the MASE array (Figure 15B), with a velocity contrast of 0.3 km/s between the low and high velocity regions. We attribute the velocity reduction to the presence of water or melt in a mantle wedge as a consequence of the subduction process. It is interesting to note that the low velocity area almost coincides with the location of volcanoes from the TMVB. Our results show a wave velocity lower than average near the location of the most recent volcanic activity (*Osete et al.,* 2000), but also at the location of older volcanoes. The fact that we cannot distinguish between old and young volcanic areas is due to the limited lateral resolution of our surface waves. The results for the bottom layer located between 100 and 200 km depth, (Figure 15C), exhibit a low velocity zone in the northern part of the

MASE array and an absence of the high shear velocities associated with the flat slab beneath the southern part of the MASE array. This can be explained by the fact that the flat part of the slab is mostly absent at this depth and its steeply dipping part at 74° is not detectable by the surface waves since it is quite thin as was shown by the P-wave tomography (*Husker and Davis,* 2009). On the other hand, the mantle wedge to the north is much wider and more detectable by Rayleigh waves and corresponds to a low velocity area. The asthenospheric low velocities beneath the TMVB are likely caused by altered mantle due to slab dehydration and/or increase in temperature in the mantle wedge. Although the slab itself is not visible as a high velocity zone, the transition to the low velocities in the north can also be used for locating the slab.

Higher velocities are seen to the west of the MASE array. This is probably explained by the large detectable size of the steeply dipping slab that crosses this zone. We note that the isodepth line at 120 km depth runs on the edge of the blue region supporting the presence of the slab. The low velocity zone to the northwest of the steep slab is close to the boundary of our well-resolved area and hence potentially suspect, but it can be associated with a possible signature of the mantle wedge associated with subduction of the Rivera slab as mentioned in *Yang et al.* (2009).

We can thus observe that the subducting slab in the study area is separated into two sections, one of which is flat and shallow (section 3, Figure 1) while the other one is steep and deep (section 2, Figure 1). An important issue is how the subduction changes across the boundary between the flat and steep portions. One possibility is that the slab is continuous, experiencing relative rapid but continuous change in subduction angle (Figure 16, bottom). Such a scenario was hypothesized by *Pardo and Suarez* (1995). However, our results on anisotropy, combined with prior studies on the ocean plate structure, age and convergence rates, as well as the slab rollback and retreat (*Mori et al.*, 2007; *Orozco et al,* 2007; *Manea et al., 2005*), point towards the scenario with a tear in the slab, as illustrated in Figure 16 (top). Note that the study area is rotated in Figure 16 relative to that of Figures 13 and 15, to give a better view of the slab morphology. The location of the transition from steep (B) to shallow (A) subduction is consistent with the location of the Orozco Fracture Zone (OFZ), which separates the older, cooler and denser oceanic crust (17.6 Ma old) from the younger oceanic crust and lithosphere (12.3 Ma old) (*Manea et al.*, 2005; *Pardo and Suarez*, 1995).

The existence of the tear is further supported by our anisotropy results. The fast directions in the mantle lithosphere and asthenosphere are, in general, parallel to the trench, except near the OFZ. In the vicinity of the OFZ they rotate to become near-parallel with the OFZ projected path, eventually deviating slightly to the west (Figure 15B and 15C). One of most likely causes of anisotropy is the flow-induced, lattice-preferred orientation of olivine. This theory is supported by a study based on P wave tomography results (*Yang et al., 2009*) that describes the mantle flow between our steep slab (B) and the Rivera slab (C) as caused by an existance of a gap between the Rivera and Cocos. Studies on GPS velocities (*DeMets et al.*, 1994) and volcanic migration (*Blatter et al.*, 2007) suggest that slab retreat and/or rollback are occurring at ~5 cm/year in our study area. The rollback/retreat should displace mantle asthenosphere and, in the presence of the slab tear, the mantle material would flow through it. The associated toroidal flows (Figure 16, top, blue arrows) would give rise to the anisotropy pattern obtained in our study (Figure 15B and 15C). The "currents" converge in front of the steep slab B, creating a characteristic line. This is similar to the explanation of the circular pattern of anisotropy in the Western US given by *Zandt and Humphreys* (2008). Note that the flow between segments A and B may also contribute to the flatness of subduction, dynamically elevating the flat slab section. We conclude that the A-B tear occurs where the plate is weakened by the presence of the fracture zone. In the back arc, the steep angle of mantle anisotropy to the strike of the arc can be explained by the flow in the mantle wedge (Figure 16, top, green arrows).

Several studies discussed the detachment of the deeper Farallon slab and its effect on the subduction structure of the region. For instance, the tomographic study of *Gorbatov and Fukao* (2005) presents evidence for the slab tear and resulting gap caused by the (30 Ma) collision of the East Pacific Rise and the coast of California. The gap widened and propagated southeastwards. On the basis of the tomographic images, they infer the present gap between the subducting Cocos plate and the Farallon slab is located much further to the north and deeper than our study area. They also proposed that the tearing is responsible for the overall shape of the Cocos subducting slab in terms of its flat and steep portions. A second more recent tear, further south, was proposed by *Ferrari* (2004) in which the Farallon slab detachment started beneath the present southern Gulf of California quickly propagating over in the southeast direction between 11.5 and 6 Ma. It would have caused migrating volcanism induced by the hot upwelling subslab asthenosphere. The proposed tear crosses our study region but would now be located at larger depths ($\sim$500 km) than we can resolve.

### 6.2. Implications for the geometry of the TransMexican Volcanic Belt (TMVB)

It is commonly pointed out that TMVB is oblique to the trench (*Ferrari*, 2004; *Pardo and Suarez*, 1995). The slab model with the tear allows for an alternative interpretation of TMVB as a combination of two segments both of which are parallel to the trench (Figure 17). One segment of the volcanic belt (B′ in Figure 17) is generated by the steeper portion of the slab (B in Figure 17), and hence it is located closer to the trench. The other segment (A′) is generated by the flatter portion of the slab and hence it is farther from the trench. Each of the segments of the volcanic belt is parallel to the trench, consistent with typical understanding of the subduction zone volcanism (*Mori et al.*, 2007). However, the difference in their distance to the trench results in what appears to be an oblique angle between the TMVB, taken as a whole, and the trench. Note that the oblique character of TMVB has already been linked to the changing subduction angle by prior studies (e.g., *Pardo and Suarez*, 1995). However, what is new in our results is the possibility that the TMVB is actually segmented.

This new interpretation allows for a natural explanation for the existence of the Tzitzio gap in volcanism (e.g., *Blatter et al.*, 2007). The gap occurs right on top of the projected path of the OFZ, and hence on top of the proposed tear in the slab structure. In this interpretation, the Tzitzio gap is simply the result of the two parallel segments that are displaced with respect to each other, as illustrated in Figure 17. The zone between them does not have steeply subducted material that would generate volcanism.

## 7. Conclusions

To investigate the structure of the Mexican subduction zone, we have constructed Rayleigh wave phase velocity maps, included the effect of the anisotropy, and inverted the results for the 3D structure of the zone in terms of shear wave velocities and their anisotropy. This detailed analysis has been possible due to the high density of stations.

The lateral variations in the isotropic part of the velocity structure in the mantle lithosphere point to the different styles of subduction on the two sides of the OFZ, with steep subduction to the northwest and nearly flat subduction to the southeast. This finding is consistent with previous studies of the structure using different methods (*Husker*, 2008; *Perez-Campos et al.*, 2008; *Iglesias et al.*, 2010; *Orozco et al.*, 2007) as well as with the two parts of the slab having different ages and hence different densities (*Blatter et al.*, 2007; *Kanjorski*, 2003; *Manea et al.*, 2006). The deeper, asthenospheric layer reveals lower velocities below the TMVB, presumably due to dehydration effects.

The anisotropy pattern is consistent with a tear between the two styles of subduction, along the OFZ, a tear between the steep Cocos and Rivera slabs, and with the associated toroidal return flows through the tears and around the steeply dipping section of the Cocos slab. This conclusion is supported by the gradual variation of the fast directions from trench-parallel near the trench to trench-perpendicular inland west of the OFZ. The flows could be caused by the slab rollback/retreat evidenced by GPS velocities and migration of TMVB (*DeMets et al.*, 1994; *Manea et al.*, 2005; *Mori et al.*, 2007).

Our hypothesis that the slab is torn allows for a new insight into the structure of the TMVB. The TMVB can be interpreted as consisting of two segments (A and B) associated with the two parts of the torn slab. Each segment is parallel to the trench, as commonly found in subduction zones. However, the two TMVB segments are located at different distances from the trench, consistent with the different angles of subduction. This creates an apparent oblique orientation of the TMVB. The segmented structure of the TMVB also provides a natural explanation for the Tzitzio gap in volcanism, which is located on top of the OFZ, where the two proposed TMVB segments are shifted with respect to each other.

**Acknowledgments.** We thank S. Lebedev of Dublin Institute for Advanced Studies, Dublin, Ireland who provided software package used to calculate the phase velocity model, and J. Arthur Snoke of Virginia Tech for the two-station method codes. Several figures were obtained using GMT software (*Wessel and Smith*, 1998). Waveform data were provided by the IRIS DMC, and the MASE, MARS, and NARS projects. Funding for this project was provided by the Center for Embedded Network Sensing (CENS) at UCLA, NSF award EAR #0609707, and the Tectonics Observatory at Caltech. The MASE experiment was funded by the Gordon and Betty Moore Foundation.

## References

Atwater, T., and J. Stock, 1998. Pacific North America plate tectonics of the Neogene southwestern United States: An update, *Int. Geol. Rev.,* 40, 375-402.

Backus, G., 1970. A geometrical picture of anisotropic elastic tensors. *Reviews of geophysics,* 8(3), 633-671.

Bassin, C., Laske, G. and Masters, G., 2000. The Current Limits of Resolution for Surface Wave Tomography in North America, *EOS Trans. AGU,* 81, F897.

Beghein, C., Snoke, J.A., and Fouch, M.J., 2010. Depth Constraints on Azimuthal Anisotropy in the Great Basin from Rayleigh Wave Phase Velocity Maps, *EPSL,* 289, 467-478.

Bevington, P.R., Robinson, D.K., 1992. Data Reduction and Error Analyses for the Physical Sciences *McGrow-Hill, New-York.*

Blatter D., Farmer G., Carmichael I., 2007. A North-South Transect across the Central MexicanVolcanic Belt at ∼100°W: Spatial Distribution, Petrological, Geochemical, and Isotopic Characteristics of Quaternary Volcanism, *Journal of Petrology,* 48, 901-950.

Brune, J., and J, Dorman, 1963. Seismic waves and earth structures in the Canadian shield, *Bull. Seism. Soc. Am.,* 53, 167-210.

Chen, T., and R. W. Clayton, 2009. Seismic attenuation structure in central Mexico: Image of a focused high-attenuation zone in the mantle wedge, *J. Geophys. Res.,* 114, B07304.

Crampin, S., Chesnokov, E. M., Hipkin, R., 1984. Seismic anisotropy; the state of the art, II, *Geophysical Journal of the Royal Astronomical Society* , vol.76, no.1, pp.1-16.

Darbyshire, F. A., Lebedev, S., 2009. Rayleigh wave phase-velocity heterogeneity and multi-layered azimuthal anisotropy of the Superior Craton, Ontario, *Geophys. J. Int.,* 176 (1), 215-234.

DeMets, C., R. G. Gordon, D. F. Argus, and S. Stein, 1994. Effect of recent revisions to the geomagnetic reversal time-scale on estimates of current plate motions, *Geophys. Res. Lett.,* 21, 2191-2194.

Dziewonski, A., Bloch, S., Landisman, N., 1969. A technique for the analysis of transient seismic signals. *Bull. Seism. Soc. Am.,* 59, 427-444.

Ferrari, L., 2004. Slab detachment control on mafic volcanic pulse and mantle heterogeneity in central Mexico, *Geology,* 32(1), 77-80.

Grand, S. P., Helmberger, D., 1984. Upper mantle shear structure of North America. *Geophysical Journal of the Royal Astronomical Society,* vol.76, no.2, 399-438.

Gorbatov, A., Fukao, Y., 2005. Tomographic search for missing link between the ancient Farallon subduction and the present Cocos subduction. *Geophys. J. Int.,* vol.160, 849-854.

Herrmann, R., 1987. Computer programs in seismology. *Tech. rep. St. Luis University,* St. Luis, Missouri.

Herrmann, R., Ammon, C., 2002. Computer programs in seismology. *Tech. rep. St. Luis University,* St. Luis, Missouri.

Husker, A. L., 2008. Tomography of the subducting Cocos Plate in central Mexico using data from the installation of a prototype wireless seismic network: Images of a truncated slab, *Ph.D. thesis,* 107 pp., Univ. of Calif., Los Angeles.

Husker, A., Davis, P., 2009. Tomography and thermal state of the Cocos plate subduction beneath Mexico City, *J. Geophys. Res.,* Vol. 114, No. B4, B04306.

Husker A., Stubailo I., Lukac M., Naik V., Guy R., Davis P., Estrin D., 2008. WiLSoN: The Wirelessly Linked Seismological Network and its application in the Middle American Subduction Experiment, *SRL* .

Iglesias, A., R. Clayton, X. Perez-Campos, S. K. Singh, J. Pacheco, D. Garcia, and C. Valdes-Gonzalez, 2010. S-Wave, Velocity Structure below Central Mexico using High Resolution Surface Wave Tomography, *J. Geophys. Res.,* 115, B06307.

Kanjorski M., 2003. Cocos Plate structure along the Middle America subduction zone off Oaxaca and Guerrero, Mexico: influence of subducting plate morphology on tectonics and seismicity, PhD thesis, University of California, San Diego.

Karato S., 1998. Seismic anisotropy in the deep mantle, boundary layers, and the geometry of mantle convection, *Pageoph* 151, 565-587.

Kennett B. L. N., Engdahl E. R., Buland R., 1995. Constraints on seismic velocities in the Earth from traveltimes, *Geophys. J. Int.,* vol.122, no.1, 108-124.

Kim, Y., Greene, F., Espejo, L., Perez-Campos, X., Clayton, R., 2006. Receiver function analysis of the Middle American subduction zone in central Mexico, *Eos Trans. AGU,* 87(52).

Knopoff L., Berry M. J, Schwab F. A., 1967. Tripartite phase velocity observations in laterally heterogeneous regions. *J. Geophys. Res.,* 72(10), 2595-2601.

Landisman, N., Dziewonski, A., Sato, Y., 1969. Recent improvements in the analysis of surface wave observations. *Geophysical Journal of the Royal Astronomical Society,* vol. 4, 369-403.

Lin, F., Ritzwoller M. H., Yang Y., Moschetti M. P., Fouch M. J., 2010. Complex and variable crustal and uppermost mantle seismic anisotropy in the western United States. *Nature Geoscience,* 4, 5561 (2010)

Londsdale, P., 1991. Structural pattern of the pacific floor offshore peninsular California, in Dauphin, J.P., and Simoneit, B.R.T. eds., The Gulf and Peninsular Province of the Californias. *American Association of Petroleum Geologists,* Memoir 47, 87-125.

Long, M. D., and P. G. Silver, 2008. The subduction zone flow field from seismic anisotropy: A global view, *Science,* 319, 315-318, doi:10.1126/science.1150809.

Manea, M., V. Manea, Luca Ferrari, V. Kostoglodov, and W. Bandy, 2005. Tectonic evolution of the Tehuantepec Ridge, *EPSL,* 238, 64-77.

Manea, V., M. Manea, V. Kostoglodov, and G. Sewell, 2006. Intraslab seismicity and thermal stress in the subducted Cocos plate beneath central Mexico, *Tectonophysics,* 420, 389-409.

Mann, P., 2007. Global catalogue, classification and tectonic origins of restraining- and releasing bends on active and ancient strike-slip fault systems, *Geol. Soc. London, Sp. Publ.,* 290.

Matsu'ura, M., and Hirata, N., 1982. Generalized least-squares solutions to quasi-linear inverse problems with a priori information, *J. Phys. Earth,* 30, 451-468.

Mori, L, Gomez Yuena, A., Cai, Y., Goldstein, S.T., 2007. Effects of prolonged flat subduction on the Miocene magmatic record of the central Trans-Mexican volcanic belt. *Chemical geology,* 244(3-4), 452-473.

Osete, M. L., Ruiz-Martinez, V. C., Caballero, C., Galindo, C., Urrutia-Fucugauchi, J., Tarling, D. H., 2000. Southward migration of continental volcanic activity in the Sierra de Las Cruces, Mexico: palaeomagnetic and radiometric evidence. *Tectonophysics,* 318, 201-215.

Orozco Esquivel, T., Petrone, C. M., Ferrari, L., Tagami, T., Manetti, P., 2007. Geochemical and isotopic variability in lavas from the eastern Trans-Mexican volcanic belt; slab detachment in a subduction zone with varying dip. *Lithos,* 93(1-2), 149-174.

Pardo, M., and Suarez G., 1995. Shape of the subducted Rivera and Cocos plates in southern Mexico: Seismic and tectonic implications, *J. Geophys. Res.,* 100, 12,357-12,373.

Perez-Campos, X., Kim, Y., Husker, A., Davis, P. M., Clayton R. W., Iglesias A., Pacheco J. F., Singh S. K., Manea V. C., and Gurnis M., 2008. Horizontal subduction and and truncation of the cocos plate beneath Central Mexico, *Geophys. Res. Lett.,* 35, L18303.

Sato, Y., 1955. Analysis of dispersed surface waves by mean of Fourier transform: Part I, *Bull. Earthquake Res. Tokyo Univ.,* 33, 33-47.

Silver, P. G., 1996. Seismic anisotropy beneath the continents: probing the depths of geology., *1081 Annu. Rev. Earth Planet. Sci.,* 24, 385-432.

Smith, M. L., Dahlen, F. A., 1973. The Azimuthal Dependence of Love and Rayleigh Wave Propagation in a Slightly Anisotropic Medium, *J. Geophys. Res.,* vol.78, no.17, 3321-3333.

Stubailo, I., Davis P., 2007. Shear wave splitting measurements and interpretation beneath Acapulco-Tampico transect in Mexico, *Eos Trans. AGU,* 88(52), Fall Meet. Suppl.

Tanimoto, T., Prindle, K., 2007. Surface wave analysis with beamforming, *Earth, Planets and Space,* vol. 59, no. 5, pp. 453-458.

Trampert, J., Woodhouse, J., 2003. Global anisotropic phase velocity maps for fundamental mode surface waves between 40 and 150 s., *Geoph. J. Int.,* 154, 154-165.

Truchan M., Larson R., 1973. Tectonic lineaments on the Cocos Plate, *EPSL,* 17, 46-432.

Turcotte, D. L. and Schubert, G., 1982. *Geodynamics: Applications of Continuum Physics to Geological Problems,* John Wiley and Sons, New York.

Warren, L., Snoke, J., James, D., 2008. S-wave velocity structure beneath the High Lava Plains, Oregon, from Rayleigh-wave dispersion inversion, *Earth Planet. Sci. Lett.,* 274, 121-131.

Wilson, D., 1996, Fastest known spreading on the Miocene Cocos-Pacific plate boundary, *Geophysical Research Letters,* v. 23, 3003-3006.

Wessel, P., and W. H. F. Smith, 1998. New, improved version of the Generic Mapping Tools released, *Eos Trans. AGU,* 79, 49, 579.

Yang, T., Grand, S. P., Wilson, D., Guzman-Speziale, M., Gomez-Gonzalez, J. M., Dominguez-Reyes, T., and Ni, J., 2009. Seismic structure beneath the Rivera subduction zone from finite-frequency seismic tomography, *J. Geophys. Res.,* vol.114, doi:10.1029/2008JB005830.

Yang, Z., Sheehan, A., Shearer P., 2011. Stress-induced upper crustal anisotropy in southern California, *J. Geophys. Res.,* vol. 116, B02302, doi:10.1029/2010JB007655.

Zandt, G., Humphreys, E., 2008. Toroidal mantle flow through the Western U.S. slab window. *Geology,* 36(4), 295-298.

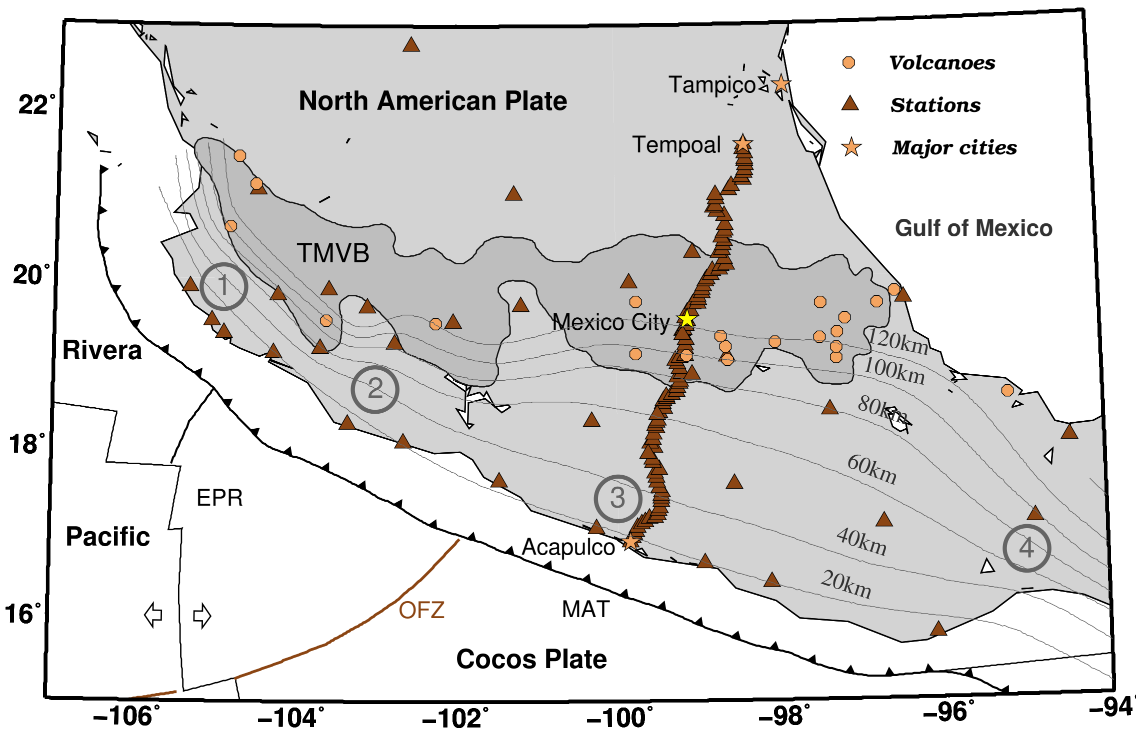


**Figure 1.** Tectonic setting of the region. The area imaged in this study is centered under the MASE array, which stretches from Acapulco to Tempoal. The MASE stations and other stations that fall within the map area are shown as triangles. The Middle America Trench (MAT), East Pacific Rise (EPR), Orozco Fracture Zone (OFZ) are also displayed. The circles represent the volcanoes that are part of the Trans-Mexican Volcanic Belt (TMVB). The isodepth lines of the Wadati-Benioff zone obtained from the local seismicity tell us that the slab is steeper in the North-West than in the South-East, and that the slab under the southern half of the MASE array is relatively flat. The circled numbers indicate the four sections of the slab geometry: (1) Jalisco, (2) Michoacan, (3) Guerrero-Oaxaca, (4) Oaxaca from *Pardo and Suarez* (1995).

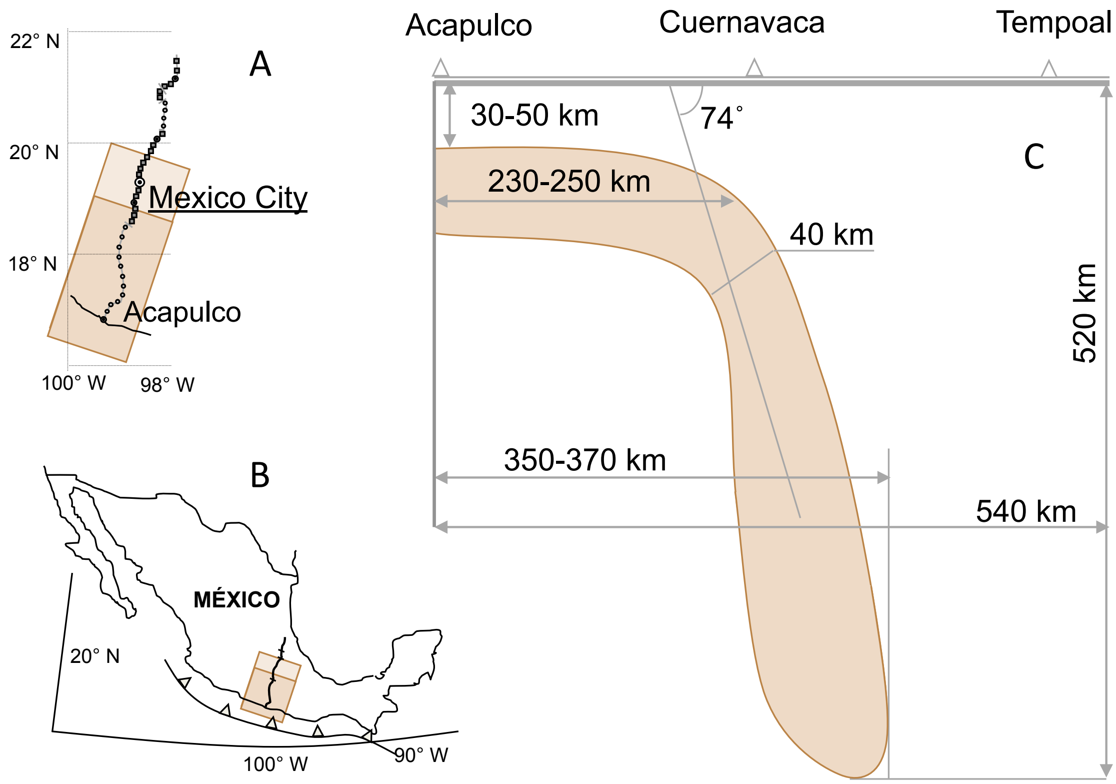


**Figure 2.** 2-D view of the slab under the MASE array based on P-wave tomography (*Husker*, 2008) and receiver function analysis (*Perez-Campos*, 2008). (A) Map view of the area showing the slab and the MASE array above it. Note the dense positioning of stations. (B) The location of the study area with respect to the trench. The study area lies within section 3 of *Pardo and Suarez* (1995). (C) The side view of the slab. The subducting slab is nearly flat for 230-250 km, and then bends relatively abruptly below the middle of the MASE array, with the subducting angle of 74°. The slab truncates at 520 km depth.

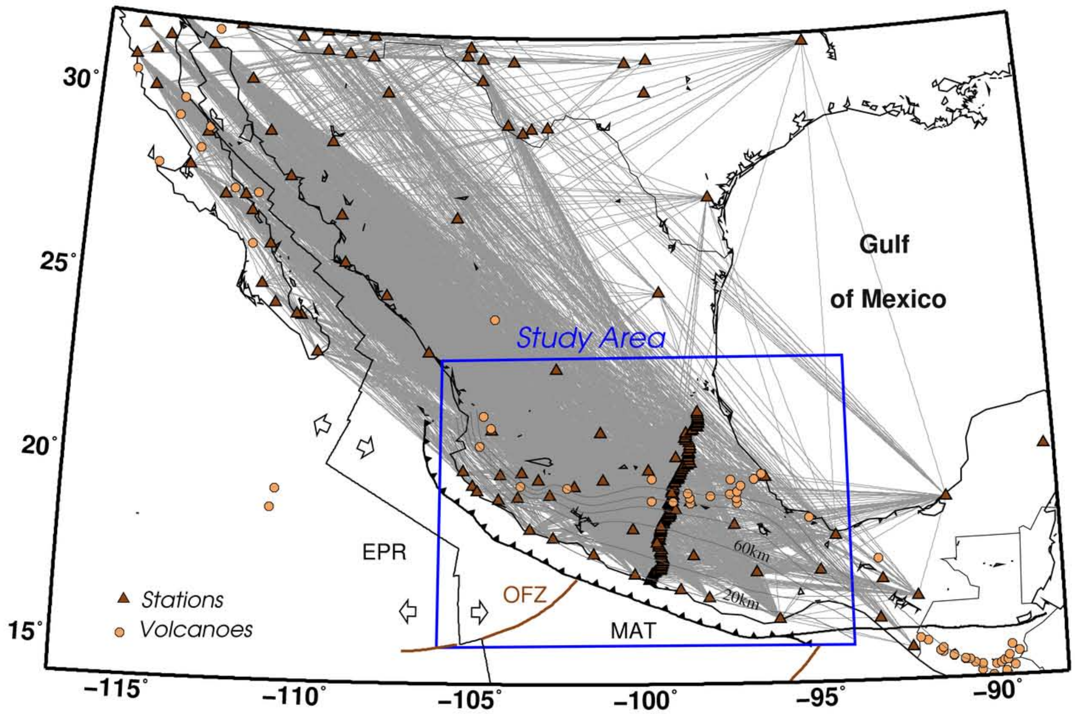


**Figure 3.** Seismic stations used in the study (triangles). The ray coverage is shown by grey lines. The area of best coverage is outlined by a blue rectangle. The circles indicate volcanoes.

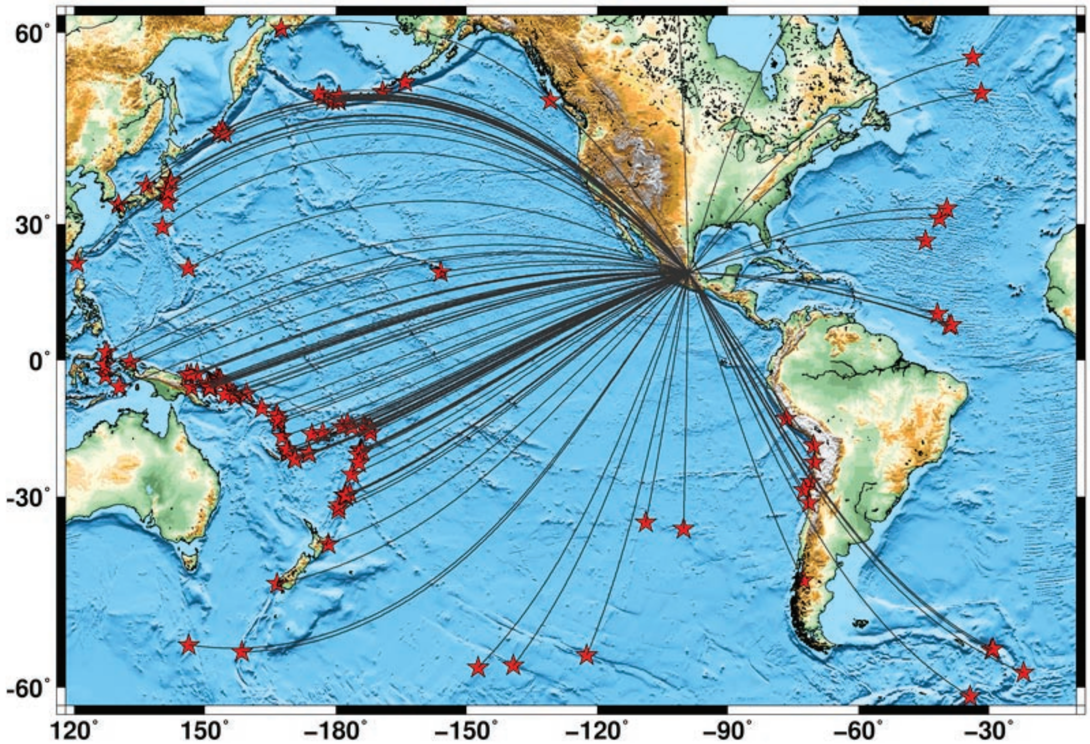


**Figure 4.** Representative events (red stars) used for the study and the corresponding great circle paths (grey lines) connecting them to a MASE array station. The chosen earthquakes are shallower than 250 km and of magnitude M $\geq$ 6.0 to have suitable signal-to-noise ratios. The events occurred between 2005/01/14 and 2009/11/13.

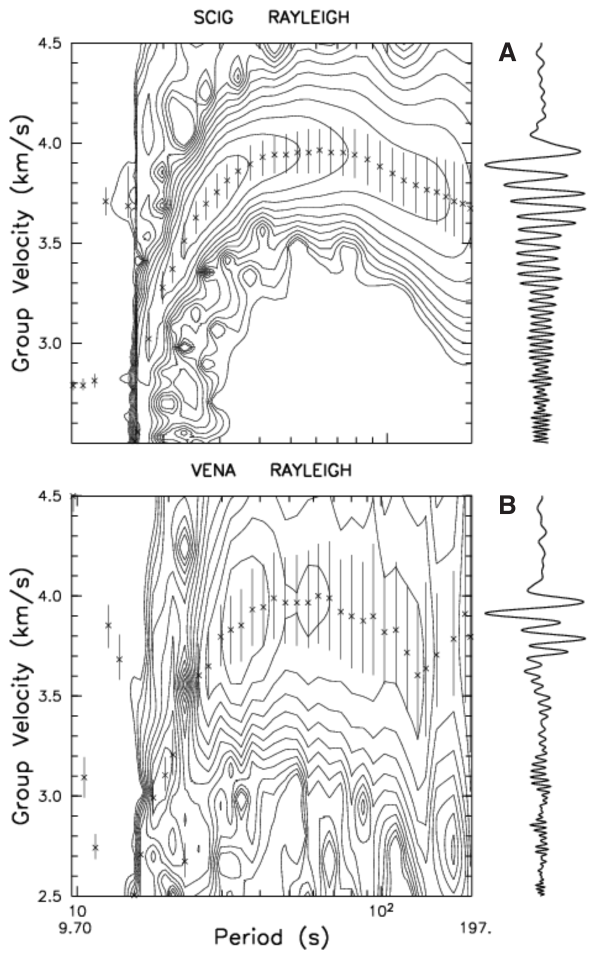


**Figure 5.** FTAN plots (*Landisman et al.*, 1969; *Dziewonski et al.*, 1969) showing single-station Rayleigh-wave group velocities *vs.* periods for the 1 March 2007 event (middle of the North Atlantic Ocean). The X symbols are computer-picked energy maxima for each period, the vertical lines span ±1 dB. Contours are placed every 3 dB. The corresponding waveforms are shown on the right sides. Panel (A) gives an example of a smooth FTAN plot for station SCIG that was used for data processing, and panel (B) shows an irregular FTAN plot for station VENA which was rejected. In (B), the contours are not smooth and well-behaved over all periods.

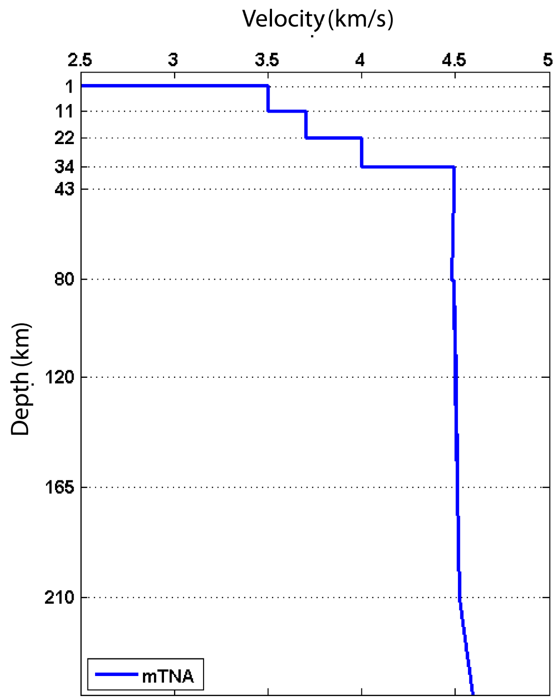


**Figure 6.** One-dimensional shear wave velocity profile used as a local reference Earth model. It is a composite model modified from the Tectonic North America (TNA) model (*Grand and Helmberger*, 1984) with the added P-wave velocities and densities from model AK135 (*Kennett et al.*, 1995), and the Crust 2.0 crustal model (*Bassin et al.*, 2000).

| depth (km) | ρ (kg/m$^3$) | Vp (km/s) | Vs (km/s) |
|---|---|---|---|
| 1.0 | 2100.0 | 2.50 | 1.20 |
| 1.0 | 2700.0 | 6.00 | 3.50 |
| 11.0 | 2700.0 | 6.00 | 3.50 |
| 11.0 | 2900.0 | 6.60 | 3.70 |
| 22.0 | 2900.0 | 6.60 | 3.70 |
| 22.0 | 3100.0 | 7.20 | 4.00 |
| 34.0 | 3100.0 | 7.20 | 4.00 |
| 34.0 | 3580.1 | 8.04 | 4.49 |
| 43.5 | 3580.1 | 8.04 | 4.49 |
| 80.5 | 3502.0 | 8.04 | 4.49 |
| 120.5 | 3426.8 | 8.05 | 4.50 |
| 165.5 | 3371.1 | 8.18 | 4.51 |
| 210.5 | 3324.3 | 8.30 | 4.52 |
| 260.5 | 3366.3 | 8.48 | 4.61 |
| 310.5 | 3411.0 | 8.66 | 4.70 |
| 360.5 | 3457.7 | 8.85 | 4.78 |
| 410.5 | 3506.8 | 9.03 | 4.87 |
| 410.5 | 3931.7 | 9.36 | 5.08 |
| 460.5 | 3927.3 | 9.53 | 5.19 |
| 510.5 | 3923.3 | 9.70 | 5.29 |
| 560.5 | 3921.8 | 9.86 | 5.40 |
| 610.5 | 3920.6 | 10.03 | 5.50 |

**Table 1.** Modified Tectonic North America model (mTNA). Figure 6 illustrates the $V_S$ velocity profile of this model.

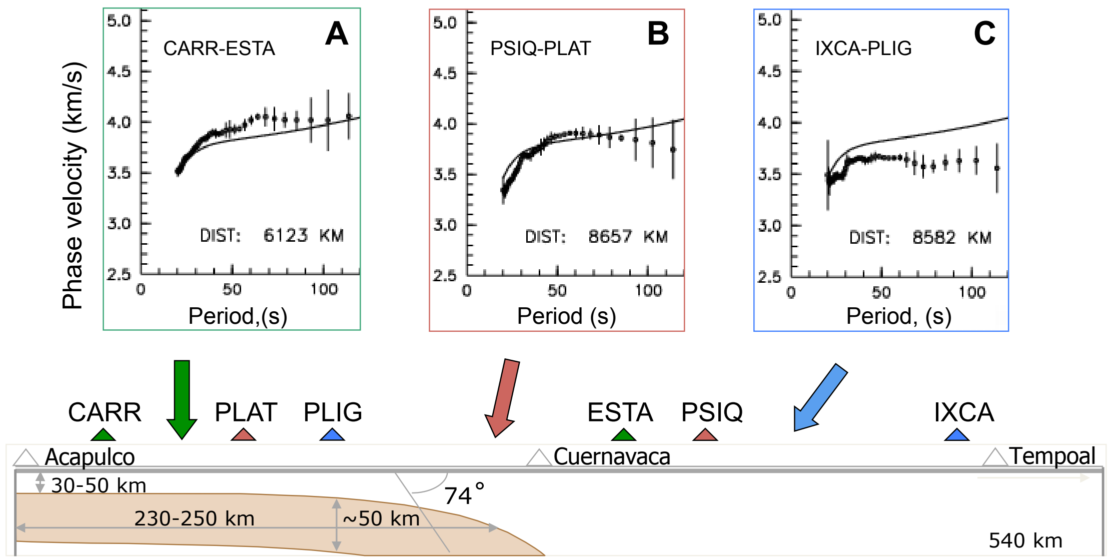


**Figure 7.** Dispersion curves along the MASE transect for three pairs of stations: (a) CARR and ESTA, located right above the slab, (b) PSIQ and PLAT, located only partially above the slab, and (c) IXCA and PLIG, located away from the slab. The location of the slab is assumed based on previous 2-D studies (e.g. *Husker and Davis* (2009)). The black dots and vertical lines give the interstation phase velocities and uncertainties measured by the two-station method. The solid lines indicate the dispersion curves predicted by the 1-D modified Tectonic North America model (mTNA). Note the systematic differences between the dispersion curves, both in terms of their departure from the 1-D model and in terms of their variation along the transect. The phase velocities above the slab are larger, and diminish while moving away from the slab, as we would expect.

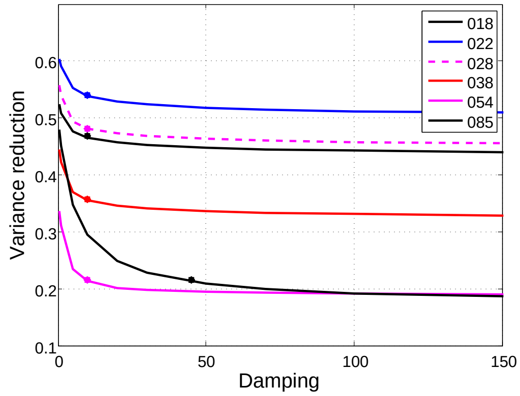


**Figure 8.** L-curves (trade-off curves) for the periods of 18, 22, 28, 38, 54, and 85 s. The L-curve displays a measure of the misfit of each model against a measure of the complexity of the model itself (damping). The dots show the points used as damping values for the preferred model; they differ for different periods.

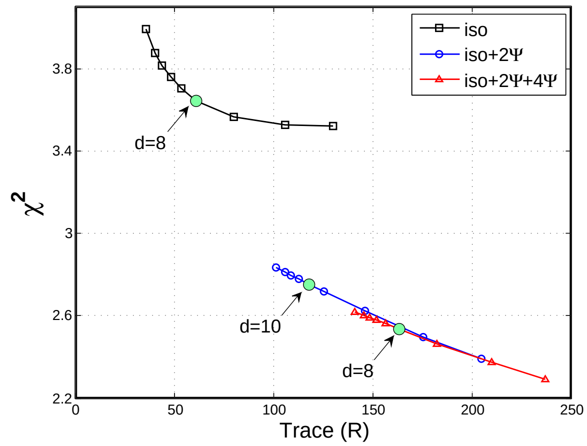


**Figure 9.** An example of reduced $\chi^2$ as a function of the trace of $\mathbf{R}$ for the isotropic (squares), isotropic and $2\Psi$ inversions (circles), and isotropic and full anisotropy of $2\Psi$ + $4\Psi$ (triangles) for the period of T=28 s. The values for the $\chi^2$ and trace are calculated for a range of damping parameters with the values of the preferred model marked by arrows. The dampings increase from right to left. We can see that the $4\Psi$ terms do not improve the fit significantly, and thus only isotropic and $2\Psi$ terms are used for anisotropic depth inversions.

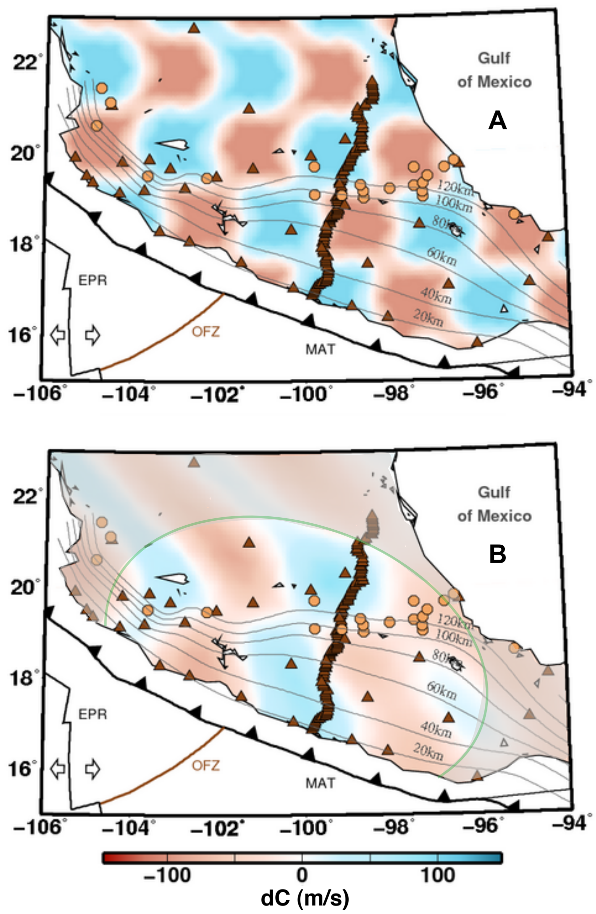


**Figure 10.** Isotropic resolution test for $T = 44\,s$. The comparison between the isotropic checkerboard input model (A) and the recovered isotropic phase velocity map (B) shows that the area around the MASE array (the non-shaded region) is well-resolved. The resolution near the MASE array is good due to the high number of the intersecting paths.

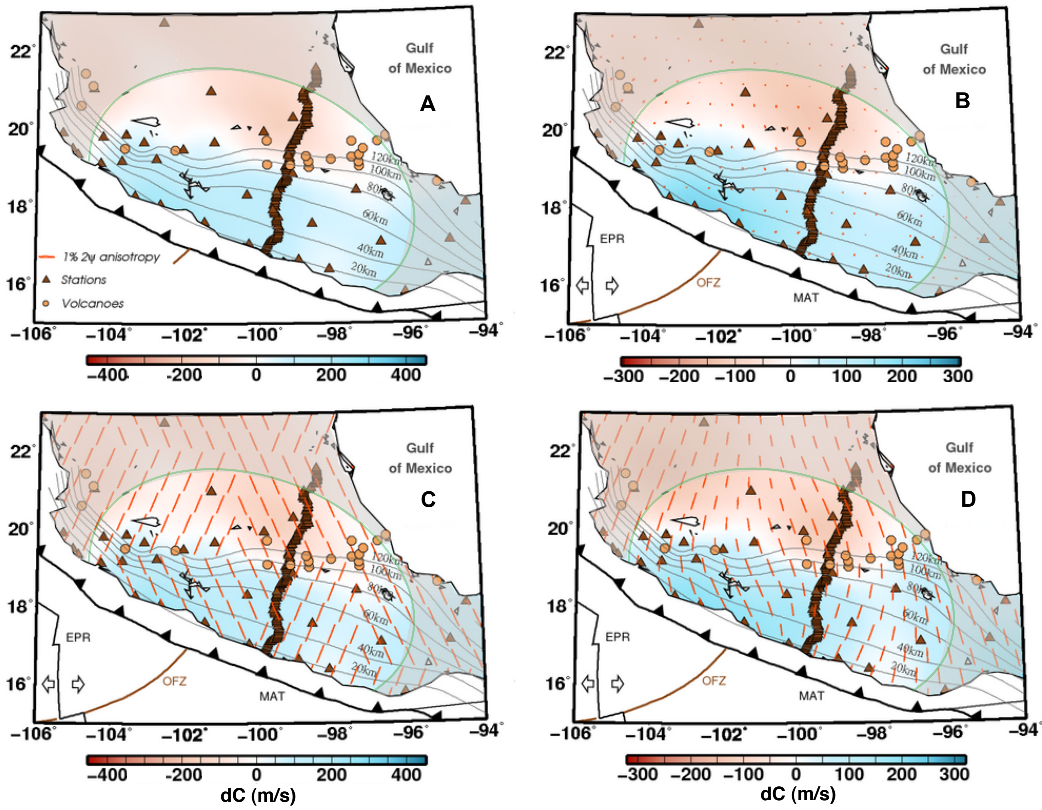


**Figure 11.** Anisotropic resolution tests for $T = 44\,s$. Panels (A) and (B) correspond to anisotropic inversions of an isotropic input model, and panels (C) and (D) show anisotropic inversions of an anisotropic input model. The input models are shown to the left and the output models are represented on the right. The input model with zero anisotropy (A) is chosen to coincide with the isotropic component of our preferred model of the region.

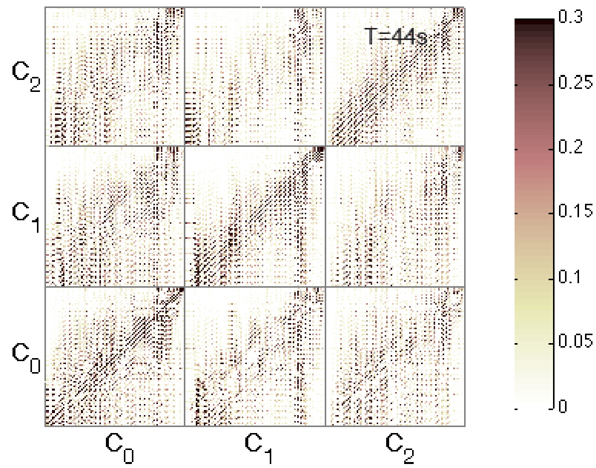


**Figure 12.** Resolution matrix for 44 s period calculated using our chosen damping. The nine submatrices represent trade-offs between the isotropic terms of the phase velocity map $c_0$, and the $2\Psi$ terms $c_1$ and $c_2$ of Eq. 2. The elements of each submatrix represent our 898 triangular grid cells. The off-diagonal submatrices indicate trade-offs between the isotropic and anisotropic terms and between the two anisotropic terms. The off-diagonal elements of the diagonal submatrices indicate lateral trade-offs, i.e. trade-offs within the isotropic or one anisotropic term at different geographic locations.

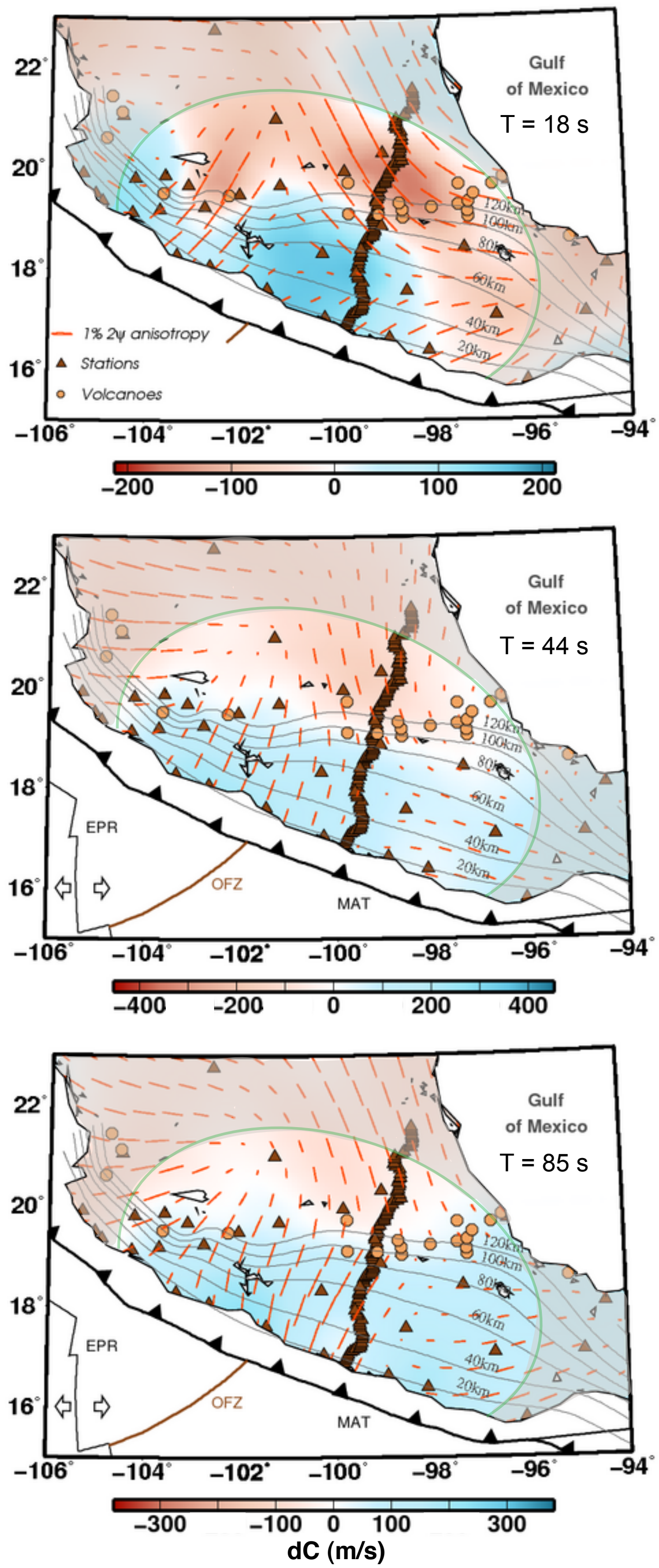


**Figure 13.** Anisotropic phase velocity maps for selected periods. The color scale represents deviations in isotropic phase velocity with respect to the phase velocity calculated for our local reference model mTNA. The red lines show both the fast direction and the magnitude of the 2Ψ-anisotropy. The non-shaded area (with the green semi-elliptical boundary) marks the well-resolved area as determined by the resolution test (Figure 10). The isolines of slab depth based on local seismicity are shown by grey lines as in Figure 1.

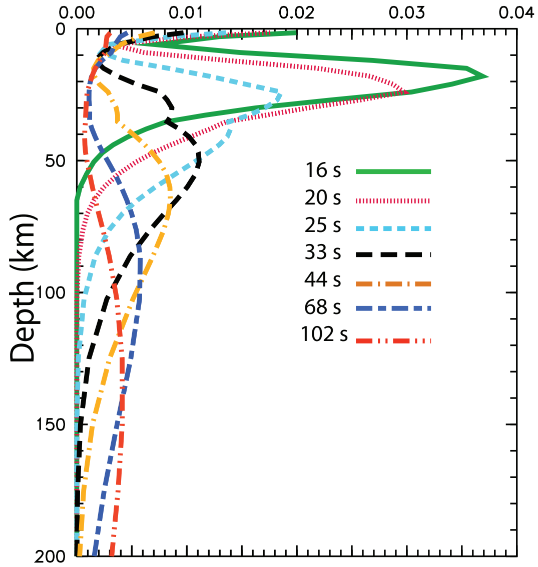


**Figure 14.** Sensitivity kernels for $V_S$ as functions of depth for several of the different periods analyzed. The kernels are the partial derivatives for fundamental-mode Rayleigh wave phase velocities with respect to $V_S$ based on the reference velocity model mTNA.

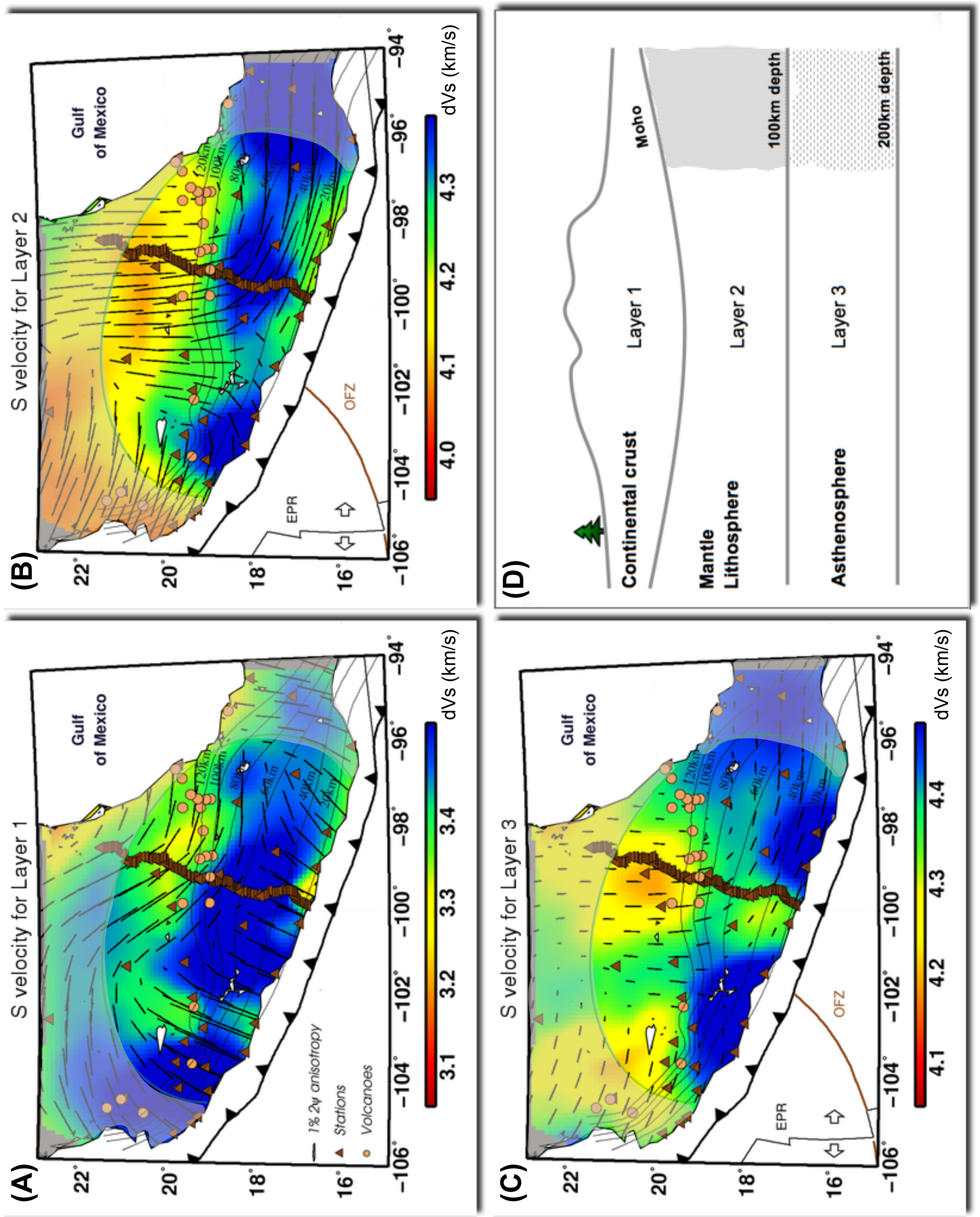


**Figure 15.** 3-D shear-wave velocity and anisotropy model based on the inversion of our Rayleigh wave phase velocity maps. (A-C) Shear-wave velocities (color) and fast directions (black dashes) averaged over each of the three layers of the model (D). Layers 1 and 2 have variable depth to account for lateral changes in crustal thickness. The velocity variations in the mantle lithosphere (layer 2) show high velocities in the subduction zone near the coast, extending inland beneath the southern part of the MASE array. These higher velocities are likely associated with the flat slab. Asthenospheric velocities (C) have low values beneath the TMVB, probably due to altered mantle from slab dehydration.

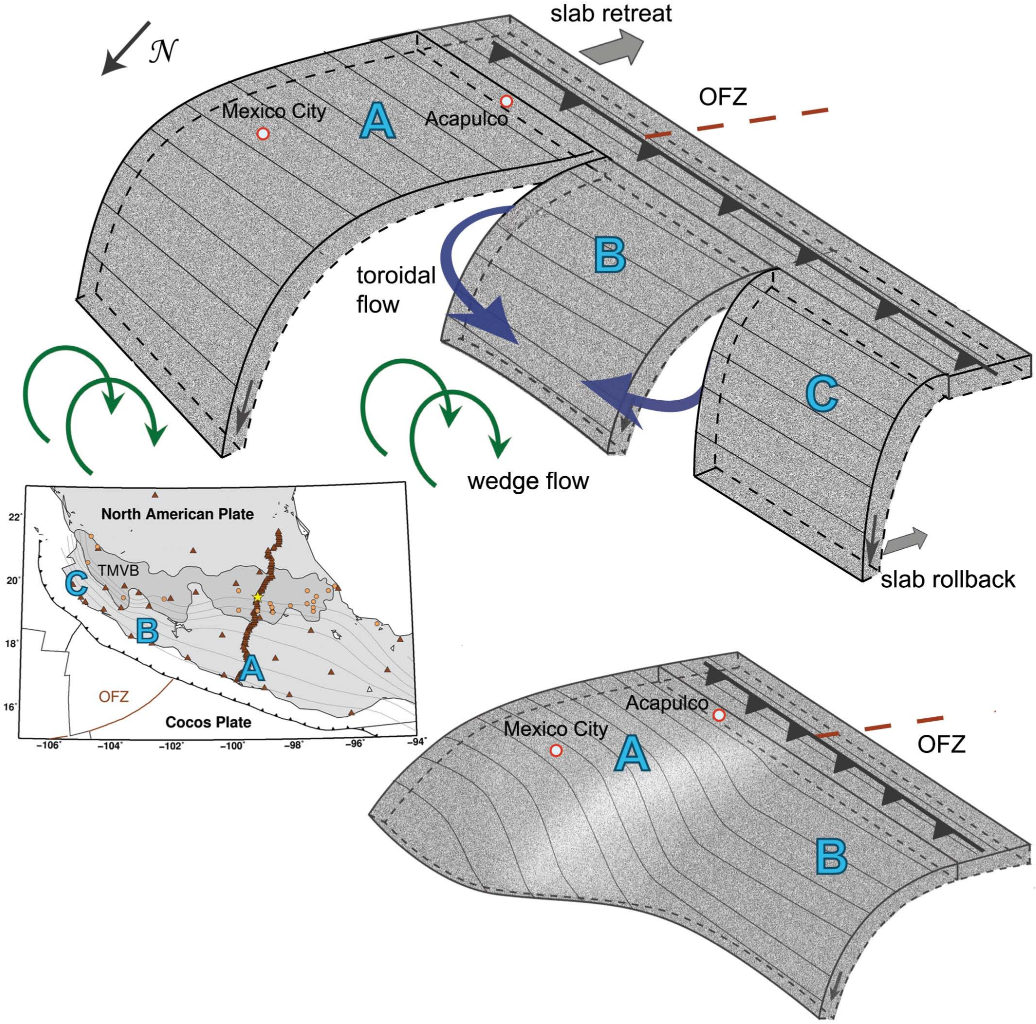


**Figure 16.** Two potential interpretations of the subduction structure in Mexico. *Top*: The flat (A) and steep (B) portions of the slab discussed in this paper separated by a tear. This is our preferred model that explains the anisotropy pattern (Figure 15). The slab retreat/rollback proposed for the area (*Mori et al.*, 2007) should displace the mantle asthenosphere, causing a toroidal flow through the tear and around the steep part of the slab (the blue arrow between A and B). The flow would explain the rotation of the fast direction in the anisotropy inversion. The tear between the two parts of the slab coincides with the projected path of the OFZ that separates the Cocos plate into areas of different ages. In addition, a mantle flow through the tear between the steep slab (B) and the Rivera slab (C) was observed in *Yang et al.*, (2009) based on P-wave tomography results. The converging flows from both sides of the steep slab B along with a wedge flow (green arrows), that has fast directions perpendicular to the trench in the back arc, explain the sharp change in the anisotropy direction line in front of the slab B (Figure 15). *Bottom*: The scenario in which the transition from the flat to steep subduction is continuous. In this scenario, the fast anisotropy direction perpendicular to the trench would be caused by the wedge flow which may be further enhanced by the slab retreat/rollback. This scenario does not explain the observed continuous rotation of the fast directions towards the OFZ that separates the two modes of subduction. *Insert*: The map view of the area with the locations of slab portions A, B, and C.

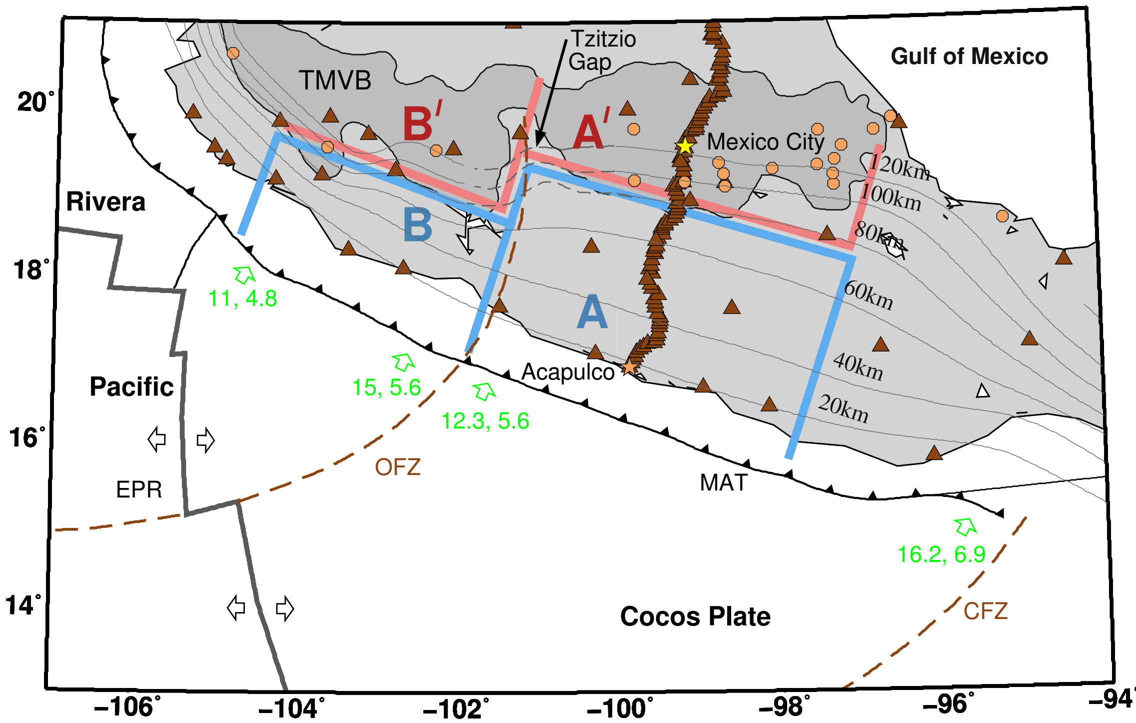


**Figure 17.** Interpretation of the TMVB structure as consisting of two trench-parallel segments. The segments (red areas A′ and B′ ) are signatures of the two segments of the subducting slab, the flat one (blue area A) and the steep one (blue area B), respectively. The two segments are independently parallel to the MAT, as typical for subduction zones, while the entire TMVB appears oblique to the MAT if the two segments are considered together. The projected path of the OFZ constitutes the boundary between the two segments. The segmented nature of the TMVB with the off-set in the distance to the trench is a natural explanation for Tzitzio gap in volcanism (*Blatter et al.*, 2007). The sketch of the area is based on *Manea et al.* (2006) and *Wilson* (1996). Triangles indicate several seismic stations used in the study, circles are the local TMVB volcanoes, OFZ, CFZ, and MAT denote Orozco Fracture Zone, Clipperton Fracture Zone, and Middle America Trench, respectively. The thick grey lines show the boundaries between tectonic plates. Green numbers are the sea floor ages in Ma and plate convergence rates in cm/year.